Earth and Planetary Science Letters 476 (2017) 143–152

Contents lists available at ScienceDirect

Earth and Planetary Science Letters

www.elsevier.com/locate/epsl

Control of serpentinisation rate by reaction-induced cracking

Benjamin Malvoisin [a,*], Nicolas Brantut [b], Mary-Alix Kaczmarek [c]

[a] ISTE-FGSE, Université de Lausanne, Quartier de la Mouline, Géopolis, CH-1015 Lausanne, Switzerland
[b] Rock and Ice Physics and Seismological Laboratory, Department of Earth Sciences, University College London, London, UK
[c] Geosciences Environment Toulouse, University Toulouse III – Paul Sabatier, Toulouse, France

ARTICLE INFO

Article history:
Received 16 May 2017
Received in revised form 21 July 2017
Accepted 25 July 2017
Available online xxxx
Editor: A. Yin

Keywords:
serpentinisation
reaction rate
reaction-induced fracturing
Marum ophiolite and Papuan ultramafic belt
mid-ocean ridges
etch pits

ABSTRACT

Serpentinisation of mantle rocks requires the generation and maintenance of transport pathways for water. The solid volume increase during serpentinisation can lead to stress build-up and trigger cracking, which ease fluid penetration into the rock. The quantitative effect of this reaction-induced cracking mechanism on reactive surface generation is poorly constrained, thus hampering our ability to predict serpentinisation rate in geological environments. Here we use a combined approach with numerical modelling and observations in natural samples to provide estimates of serpentinisation rate at mid-ocean ridges. We develop a micromechanical model to quantify the propagation of serpentinisation-induced cracks in olivine. The maximum crystallisation pressure deduced from thermodynamic calculations reaches several hundreds of megapascals but does not necessary lead to crack propagation if the olivine grain is subjected to high compressive stresses. The micromechanical model is then coupled to a simple geometrical model to predict reactive surface area formation during grain splitting, and thus bulk reaction rate. Our model reproduces quantitatively experimental kinetic data and the typical mesh texture formed during serpentinisation. We also compare the model results with olivine grain size distribution data obtained on natural serpentinised peridotites from the Marum ophiolite and the Papuan ultramafic belt (Papua New Guinea). The natural serpentinised peridotites show an increase of the number of olivine grains for a decrease of the mean grain size by one order of magnitude as reaction progresses from 5 to 40%. These results are in agreement with our model predictions, suggesting that reaction-induced cracking controls the serpentinisation rate. We use our model to estimate that, at mid-ocean ridges, serpentinisation occurs up to 12 km depth and reaction-induced cracking reduces the characteristic time of serpentinisation by one order of magnitude, down to values comprised between 10 and 1000 yr. The increase of effective pressure with depth also prevents cracking, which positions the peak in serpentinisation rate at shallower depths, 4 km above previous predictions.

1. Introduction

Olivine is the main constituent of upper mantle rocks. Under hydrothermal conditions olivine reacts with water to form serpentine and brucite, which are hydrous phases. This replacement reaction, commonly termed serpentinisation, is promoted by tectonic deformation exposing mantle rocks (peridotites) on the Earth's surface at mid-ocean ridges and in ophiolites. The serpentinisation of olivine modifies mantle rocks rheology (Escartín et al., 2001), geochemical water cycle (Rüpke et al., 2004) and the thermal structure of the lithosphere (Allen and Seyfried, 2004). Moreover, the iron contained in olivine can be partly oxidized to form magnetite and hydrogen (Moody, 1976), with first-order consequences for the formation of extremely reducing environment (Frost, 1985) and the magnetic signal recorded in the oceanic lithosphere (Toft et al., 1990; Sleep et al., 2004).

All these changes in physico-chemical properties associated with serpentinisation depend on the reaction rate. Replacement reactions such as serpentinisation can be decomposed in four successive steps: (1) transport of fluids to olivine, (2) olivine dissolution, (3) transport of aqueous species and (4) precipitation of serpentine. Hydrothermal experiments on olivine powders have shown that dissolution and precipitation (steps 2 and 4) are fast compared to the transport of fluid and aqueous species (steps 1 and 3). The transport steps are thus controlling the reaction rate (Martin and Fyfe, 1970; Wegner and Ernst, 1983; Seyfried et al., 2007; Malvoisin et al., 2012). Diffusion at grain junctions is slower than olivine dissolution at temperature below 350 °C (Malvoisin and Brunet, 2014). Therefore, fractures are the main fluid pathways involved during serpentinisation. Because the solid volume

* Corresponding author.
E-mail address: benjamin.malvoisin@unil.ch (B. Malvoisin).

http://dx.doi.org/10.1016/j.epsl.2017.07.042

increases by approximately 50 % during serpentinisation, fractures can be clogged be reaction products, inducing a decrease in peridotite permeability (Macdonald and Fyfe, 1985; Hövelmann et al., 2012; Godard et al., 2013; Farough et al., 2016). However, this clogging is not complete, as shown by the preservation of a porosity of several percent in natural serpentinised peridotites (Tutolo et al., 2016). At the kilometre to the metre scale, fracture networks are mainly formed by tectonic deformation (Tucholke and Lin, 1994; Tauzin et al., 2017). By contrast, at the grain scale, thermal contraction, stress build-up due to the reaction, and preferential dissolution along sub-grain boundaries and other flaws (Malvoisin et al., 2012; Plümper et al., 2012; Klein et al., 2015; Lisabeth et al., 2017) are the main processes invoked for the generation of the observed mesh textures, characterised by polygonal olivine grains surrounded by serpentine veins (Wicks and Whittaker, 1977). Thermal cracking is associated with fast tectonic exhumation and associated temperature decrease in peridotites (Boudier et al., 2010). Demartin et al. (2004) provided a micro-mechanical model and experimental constraints for thermal cracking in peridotites. In addition to thermal effects, the positive solid volume change during serpentinisation also generates stresses (i.e., crystallisation pressure) sufficient to fracture the rock (Macdonald and Fyfe, 1985; Iyer et al., 2008; Kelemen and Matter, 2008; Jamtveit et al., 2009). It is still not clear if fluid pathways generation in natural samples is controlled by thermal or reaction-induced cracking. Based on evidences of hierarchical fracturing in orthopyroxenite dykes from Leka ophiolite (Norway), Iyer et al. (2008) proposed that reaction-induced fracturing is the main process forming fluid pathways during serpentinisation while Boudier et al. (2010) used olivine preferred orientation to show that thermal contraction controls cracking in peridotites from Oman. Rouméjon and Cannat (2014) proposed a mixed scenario for serpentinised peridotites from mid-ocean ridges with microfractures formed by thermal cracking serving as a basis for fracture network densification by reaction-induced cracking. However, quantitative estimates of the influence of the two fracturing processes on reactive surface area generation are still lacking to predict their influence on serpentinisation rate.

The crystallisation pressure has been extensively studied at ambient temperature for monophasic systems such as ice or salts through experimental and theoretical works (e.g., Steiger, 2005). The proposed theory is based on the presence of a constantly renewed nanometre scale liquid film at the rock surface to both supply ions for crystal growth and allow the crystal to perform mechanical work (e.g. Røyne et al., 2011). The simplest way to model reaction-induced cracking is to relate directly fracturing to the reaction progress, typically by using a critical stress criterion for fracture opening. This approach allows to investigate qualitatively the influence of reaction-induced fracturing on reaction front propagation (Rudge et al., 2010) and on the generated fracture patterns (e.g. Jamtveit et al., 2009; Kelemen and Hirth, 2012; Plümper et al., 2012). Despite the overall success of these models in reproducing the phenomenological features associated with reaction-induced fracturing, quantitative comparisons of model outputs with both texture evolution and bulk reaction rate are still missing.

Here, we propose to bridge this gap by developing a grain-scale model accounting for the feedbacks between reaction kinetics, crystallisation pressure and fracture mechanics. Our micromechanical approach minimizes the use of phenomenological parameters and allows to make actual predictions of bulk reaction rate and texture evolution, which are compared to published experimental data (Malvoisin et al., 2012) and to new measurements on peridotites from the Marum ophiolite and the Papuan ultramafic belt (Papua New Guinea) serpentinised at low temperature (Kaczmarek et al., 2015).

2. Observations in natural samples

2.1. Image analysis of variably serpentinised peridotites

Here we aim to investigate mineralogical processes occurring during serpentinisation in natural samples, and extract the evolution of grain size, shape and number density as a function of reaction progress. We use ophiolitic samples from the Marum ophiolite and the Papuan ultramafic belt (PUB; Papua New Guinea) including pristine, moderately and extensively serpentinised peridotites, with reaction progress ranging from only a few percents up to more than 95%. The ophiolite was obducted during the convergence between the Australian and the Pacific plates (Lus et al., 2004) and subsequently serpentinised during its exposure at the surface.

Fifteen samples of variably serpentinised peridotites from the Marum ophiolite and the PUB are selected for petrological study and image analysis (Table S1). Mineral chemistry and backscattered electron (BSE) images are performed with a Tescan Mira LMU (JEOL) field-emission scanning electron microscope operated at 20 kV and 23 mm working distance and equipped with an EDS detector from Oxford Instrument at the University of Lausanne. Serpentine mineralogy is characterised by Raman microspectrometry using a Horiba LabRAM HR800 microspectrometre equipped with a 532.1 nm laser at the University of Lausanne. In each sample, we use optical microscopy observations to select one to four olivine-rich and pyroxene-free zones, ranging from 2.3 to 11.7 mm in size, for image analysis. This results in a total of 37 zones containing one or several olivine crystals fragmented by micro-cracks. Each of these zones is mapped by acquiring between 18 and 464 BSE images (depending on the size of the zone). For each zone, BSE images are then stitched together to reconstruct a mosaic image with a resolution ranging between 0.54 and 0.67 µm per pixel (Fig. S1 a and d). We use a gray scale criterion and dilation/erosion techniques to automatically attribute each pixel to either (1) olivine, (2) serpentine and/or brucite, or (3) other phases (e.g., magnetite, spinel or epoxy). The measured surface area of serpentine is converted into an amount of reacted olivine by using the olivine/(serpentine + brucite) volumetric ratio (0.68), allowing us to obtain the reaction progress.

Binary images are then produced with olivine pixels only (Fig. S1 b and d) and then segmented in order to associate pixels from the same grain (Fig. S1 c and f). Finally, bounding rectangles with the minimal surface area are adjusted to each grain contour in order to retrieve grain size and orientation (Fig. S1 c and f). Olivine grains smaller than 5 µm are not considered for statistical analysis due to the lack of resolution below this size. The final number of grains identified in each zone is between 287 and 36,537 (Table S1) which is above the limit of approximately 200 grain sections necessary for statistical analysis (Malvoisin et al., 2012). In the following, the grain size refers to the mean of the sizes of the long and short sides of the minimal bounding rectangle. Grain orientation refers to the angle between the horizontal and the side of the bounding rectangle crossing the first quadrant of the unit circle (0 to 90°). For statistical analysis on grain orientation, groups of grains with close crystallographic orientations are defined by using polarised light microscopy with which grains associated to the same primary olivine crystal have similar optical properties. For each of these groups, angle mean values and standard deviations are determined by using circular statistics (Fisher, 1993).

2.2. Morphological properties of residual olivine grains

The natural samples from the PUB are dunites, while peridotite samples from the Marum ophiolite are dunite, harzburgite and

wehrlite (Table S1). A detailed description of the primary mineralogy can be found in Kaczmarek et al. (2015). Olivine has a Mg/(Mg+Fe) ratio comprised between 0.89 and 0.93. Serpentinisation degree estimates based on image analysis in these samples range from 5 to 97% (Table S1). Serpentine and magnetite are observed as serpentinisation products in all the samples. All the Raman spectra collected in the samples show at high-frequencies a major band at 3685 cm^{-1} and a less intense band at 3703 cm^{-1} indicating the presence of lizardite (Auzende et al., 2004). Magnetite is typically found as micron-sized isolated grains. Brucite with a high iron content (atomic Mg/(Mg+Fe) ratio comprised between 0.61 and 0.82; Table S1) is found in the dunites. The small amount of magnetite and the high iron content of brucite indicates serpentinisation at temperature below 200 °C (Malvoisin et al., 2012), which is commonly observed in ophiolitic settings (Klein et al., 2014).

The peridotites have a porphyroclastic texture with primary olivine crystals ranging in size from 1 mm to 12 mm. Even at low reaction progress, these crystals are fragmented into grains by microcracks resulting in a mesh texture (Fig. 1 a and b). At the surface of these grains, 1 to 15 µm-wide etch pits are formed resulting in sawtooth boundaries of grain sections (Fig. 1 c, d and f). Micro-cracks initiate from etch pits (Fig. 1 c, d and f). Successively, etch pits develop on micro-cracks walls allowing for a new generation of micro-cracks to form (Fig. 1 h). This sequential process results in hierarchical fracturing (Fig. 1 e and f). In the less altered samples, this process is enhanced at olivine/spinel grain boundaries leading to radial cracking around spinels (Fig. 1 g and h).

The mean grain size and the grain size weighted by grain surface area (WMGS) decrease from approximately 50 and 500 µm at 5% reaction progress to approximately 20 and 60 µm at 80% reaction progress, respectively (Fig. 2 a and b). The decrease in olivine grain size is not linear with reaction progress, and occurs most rapidly during incipient serpentinisation, for reaction extents below 30%. From 80 to 97% reaction progress, the WMGS is rather constant whereas the mean grain size increases from approximately 20 to 30 µm due to complete reaction of the smallest grains.

The evolution of the number of grains with reaction progress displays a bell-shaped curve (Fig. 2 c). The number of grains increases from 100 to approximately 700 grains/mm^2 as the reaction progresses from 5 to 40%. Beyond 40% serpentinisation, the number of grains decreases with reaction progress to reach a minimum value of around 20 grains/mm^2 at 97% serpentinisation.

The grain orientation distribution indicates that grains can have a shape preferred orientation at reaction extents up to approximately 70% (Fig. S2). The measurement of a single shape preferred orientation indicates that the cracks surrounding the residual olivine grains are oriented at approximately 90° to each other. At 97% of reaction, no preferred orientation can be determined (Fig. S2 k). The standard deviation of grain orientations was used to determine if the grains have a preferred orientation. This standard deviation ranges from approximately 10 to 20° and preferred orientation is difficult to determine for standard deviation above 18° (Fig. S2 j). Grain populations with no shape preferred orientation (standard deviation above 18°) are found in samples with reaction progresses above 50% (Fig. 2 d).

3. Crack growth from serpentinisation: microscale model

Our microstructural observations show that microcracks in olivine propagate from surface etch pits, in which serpentine precipitates. In this Section, we develop a microscale model based on linear elastic fracture mechanics to compute the rate of fracture propagation as serpentinisation proceeds.

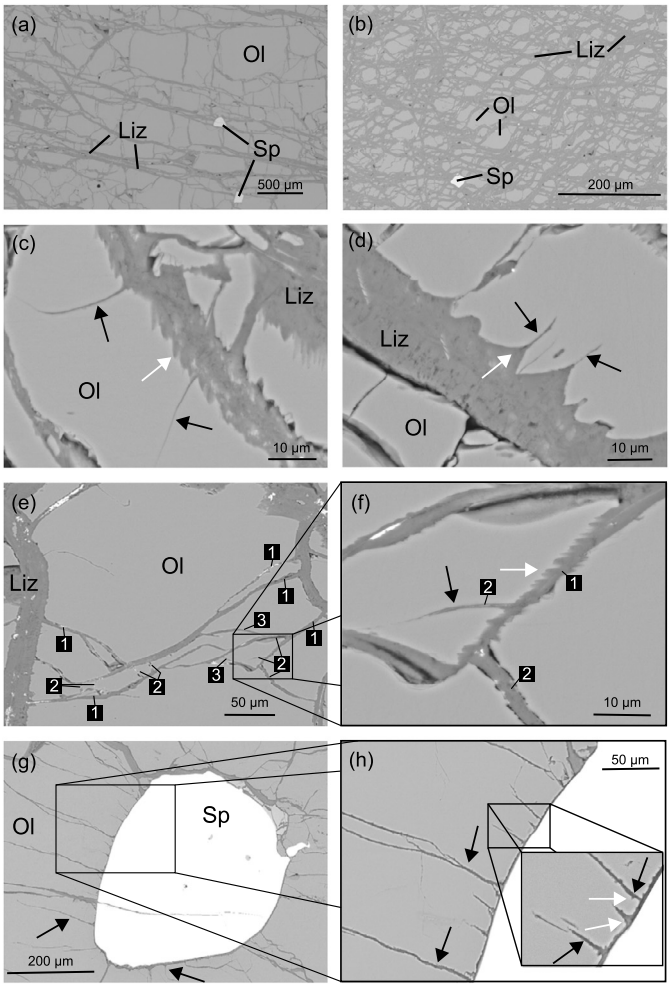

Fig. 1. Backscattered electron images of olivine grain (Ol) partially replaced by lizardite (Liz) in samples from the Marum ophiolite and the PUB. (a) and (b): Mesh textures in samples B24 and A2c, respectively. (c) and (d): Micro-cracks (black arrows) initiate from etch pits (white arrows; (c) and (d), respectively). (e) and (f): Etch pits formation on micro-cracks walls leads to new micro-cracks formation. The repetition of this process in time results in hierarchical fracturing of olivine grains. At least three successive fracture generations numbered from 1, for the oldest one, to 3, for the youngest one, can be identified. (g) and (h): Enhanced etch pits formation at spinel (Sp)/olivine interface resulting in radial fracturing around spinel. The formation of a second generation of etch pits on fracture walls is highlighted on panel (h).

3.1. Model description

Let us consider the surface of an olivine grain during the serpentinisation process, in the simplified geometry depicted in Fig. 3. The etch pits forming at the surface of the olivine grain during the early stage of the reaction (e.g. Malvoisin et al., 2012; Plümper et al., 2012) act at initial surface notches, and the precipitation of serpentine in these etch pits generates a wedging stress promoting the propagation of a fracture from the bottom of the pits. In the two dimensional configuration shown in Fig. 3, the serpentine "wedge" has a length a and a width w, and we model the etch pit and the associated fracture by an edge crack of length c. The normal stress generated by the precipitation of serpentine is denoted σ_n, and we account for a far-field compressional effective stress σ'_∞ acting normal to the edge crack, transmitted through the solid skeleton of the olivine aggregate.

In the edge crack, serpentine growth is driven by a difference in chemical potential $\Delta_r G$ that is function of the serpentine precipitation reaction quotient Q_{prec} and the normal stress σ_n acting on the serpentine wedge:

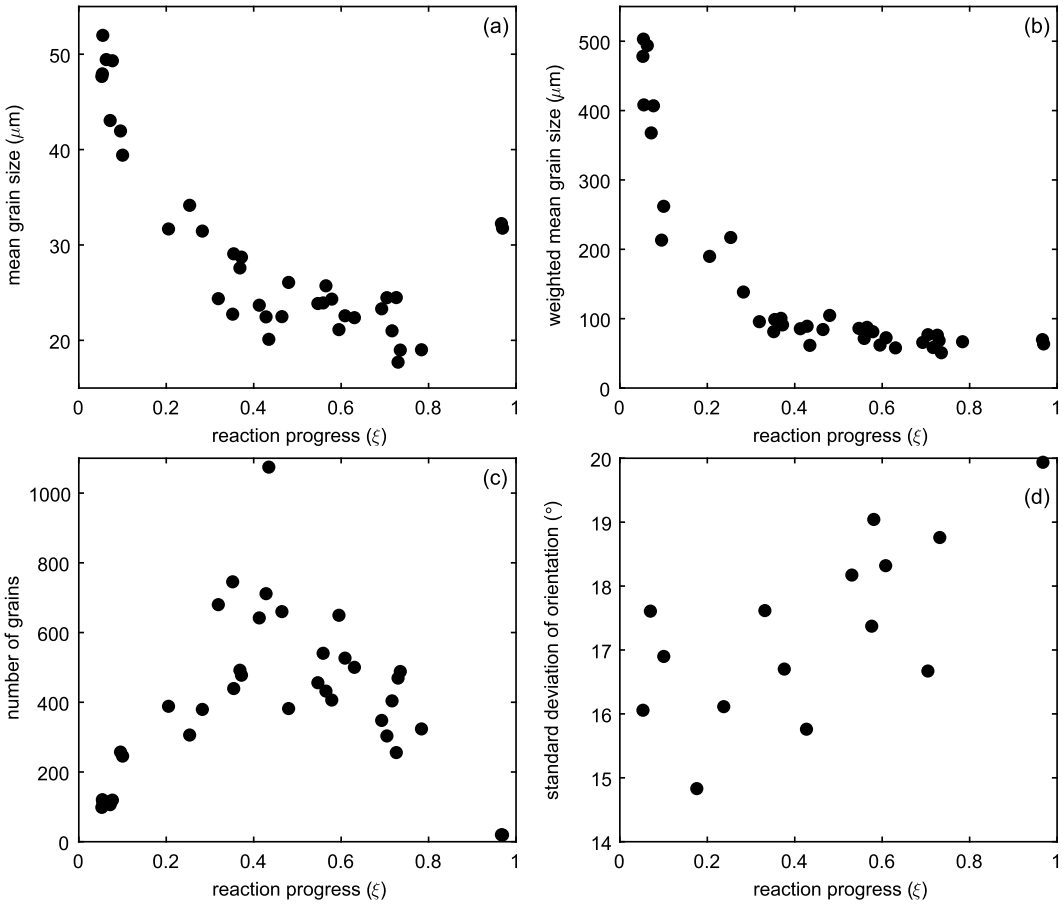

Fig. 2. Residual olivine grain morphological properties as a function of reaction progress for selected zones in samples from the Marum ophiolite and the PUB. (a) Mean grain size. (b) Mean grain size weighted by grain surface area. (c) Number of grains per surface unit area. (d) Standard deviation of grain shape orientation compared to the mean grain orientation for each sample.

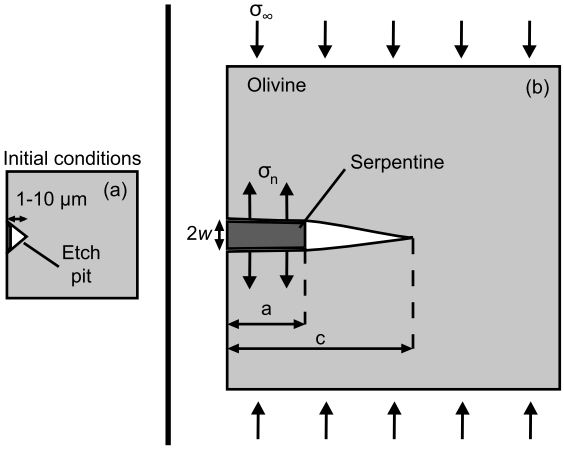

Fig. 3. Geometry of crack propagation model. (a) Initial conditions. The pre-existing fracture is assumed to be an etch pit formed by anisotropic olivine dissolution. (b) Geometry for crack propagation as serpentine precipitates into the crack. a and w are the length and half-width of the serpentine mineral. c is the crack length.

$$\Delta_r G = -RT \log Q_{prec}/K_{prec} + \sigma_n V_m, \tag{1}$$

where R is the gas constant, T is the temperature, K_{prec} is the reaction quotient at a stress-free chemical equilibrium, and V_m is the molar volume of serpentine.

Serpentine precipitation results from the increase in aqueous species activities due to olivine dissolution and leading to serpentine supersaturation, expressed here with the degree of supersaturation $\Omega = K_{prec}/Q_{prec}$. At fixed Ω, the system will either constantly react if it is unconfined, or it will tend towards equilibrium if the normal stress can increase up to the crystallisation pressure σ_c, given by

$$\sigma_c = \frac{RT}{V_m} \log \Omega. \tag{2}$$

Eq. (2) is equivalent to the formulation proposed by Correns (1949), Steiger (2005) and Kelemen and Hirth (2012) for calculating crystallisation pressure. It assumes a complete conversion of the chemical potential energy into pressure change. Paterson (1973) and Kelemen and Hirth (2012) noted that this is only true at first-order since the chemical energy can also contribute to small elastic strain energy and heat productions. The crystallisation pressure calculated with Eq. (2) is thus a maximum.

For a given driving force $\Delta_r G$, the rate of serpentine crystal growth (denoted r, with units of $m\,s^{-1}$) is given by (Lasaga, 1981):

$$r = k\left(1 - \exp\left(\frac{\Delta_r G}{RT}\right)\right)^{\kappa}, \tag{3}$$

where k is a kinetic constant (with units of $m\,s^{-1}$) that accounts for the effect of temperature on reaction rate, and κ is an empirical exponent. Assuming $\kappa = 1$, for small departures from equilibrium, the expression (3) can be approximated by

$$r \approx \frac{kV_m}{RT}(\sigma_c - \sigma_n). \tag{4}$$

Given the geometry assumed in Fig. 3, the rate of growth in length da/dt of the serpentine wedge is that of an unconfined face,

$$\frac{da}{dt} = K\sigma_c, \tag{5}$$

and the rate of growth in width dw/dt is that of a confined face,

$$\frac{dw}{dt} = K(\sigma_c - \sigma_n), \tag{6}$$

where $K = (kV_m)/(RT)$.

The evolution of the total edge crack length c is given by a Griffith criterion, i.e., the crack propagates when the energy release rate G reaches the critical energy release rate G_c. The energy release rate at the crack tip is given by

$$G = K_I^2/E', \tag{7}$$

where K_I is the mode I stress intensity factor and $E' = E/(1-\nu^2)$, where E is Young's modulus and ν is Poisson's ratio of the olivine grain. For an edge crack wedged by a normal stress σ_n over a distance a and under remotely applied compressive stress σ'_∞, the stress intensity factor is expressed as (Tada et al., 2000):

$$K_I = \frac{2\sqrt{c}}{\sqrt{\pi}}\left(\gamma\left(\frac{a}{c}\right)\sigma_n - \mu\sigma'_\infty\right), \tag{8}$$

where $\gamma(a/c)$ is a known function (Tada et al., 2000), and $\mu = 1.1215 \times (\pi/2)$. Substituting K_I into Eq. (7), we obtain the following expression for the energy release rate:

$$G = \frac{4c}{\pi E'}\left(\gamma\left(\frac{a}{c}\right)\sigma_n - \mu\sigma'_\infty\right)^2. \tag{9}$$

The opening displacement at the surface is given by Tada et al. (2000)

$$\frac{w}{c} = \frac{1}{E'}\left(\lambda\left(\frac{a}{c}\right)\sigma_n - \theta\sigma'_\infty\right), \tag{10}$$

where $\lambda(a/c)$ is also a known function (Tada et al., 2000), and $\theta = 2.908$. Therefore, for a given crack and wedge geometry, the normal stress on the wedge is given by

$$\sigma_n = \frac{E'}{\lambda(a/c)}\frac{w}{c} + \frac{\theta}{\lambda(a/c)}\sigma'_\infty. \tag{11}$$

The fully coupled reaction and crack growth problem consists in determining the geometrical parameters a, w, and c as a function of time. The evolution of a and w is given by the pair of ordinary differential equations (5) and (6), and we compute the evolution of c as:

$$\frac{dc}{dt} = \begin{cases} da/dt & \text{if } G < G_c \text{ and } a = c, \\ 0 & \text{if } G < G_c \text{ and } a < c, \\ f(a,c,w) & \text{if } G = G_c, \end{cases} \tag{12}$$

where $f(a,c,w)$ is obtained from the condition that crack growth occurs to maintain $dG(a,c,w)/dt = 0$ (i.e., G is constant, equal to G_c):

$$f(a,c,w) = \frac{1}{\partial G/\partial c}\left(\frac{\partial G}{\partial a}\frac{da}{dt} + \frac{\partial G}{\partial w}\frac{dw}{dt}\right). \tag{13}$$

The expression (12) ensures that $c = a$ while serpentinisation proceeds as long as the fracture criterion is not yet reached.

3.2. Behaviour of a single crack

We first examine the growth of a single crack in an olivine grain, resulting from the precipitation of serpentine in a preexisting surface etch pit. For olivine, we use $E' = 208$ GPa (Abramson et al., 1997) and $G_c = 2$ J m^{-2} (Atkinson, 1984). The crystallisation stress σ_c is a function of the fluid supersaturation, and varies with fluid pressure, temperature and fluid composition. In natural systems these parameters are not known although they play a key role on deformation. Fletcher and Merino (2001) assumed a small supersaturation during a replacement reaction to calculate the stress state in an elastic rock. Such an approach cannot be used here since serpentinisation occurs at conditions far from the equilibrium and can thus generate high crystallisation stresses. As a first approximation we use the approach of Kelemen and Hirth (2012) and compute the supersaturation by assuming that the fluid is at thermodynamic equilibrium with both the reactants and the products. In this assumption, the supersaturation Ω is equal to the equilibrium constant K_{eq} of the serpentinisation reaction, which provides an upper bound for the crystallisation stress. The constant K_{eq} was calculated for a range of fluid pressures and temperatures with SUPCRT92 (Johnson et al., 1992) for the following reaction:

$$\text{Forsterite} + \text{Enstatite} + 2H_2O \rightleftharpoons \text{Chrysotile}. \tag{14}$$

This equation is based on the compilation of compositions given by Malvoisin (2015) showing brucite scarcity in serpentinised peridotites due to the presence of silica-rich fluids formed during pyroxenes reaction. Fig. 4 shows how the resulting stress σ_c evolves as a function of temperature: it typically ranges from around 100 MPa at 350 °C up to more than 350 MPa at 100 °C. Such stresses are consistent with previous estimates for similar reactions by Kelemen and Hirth (2012).

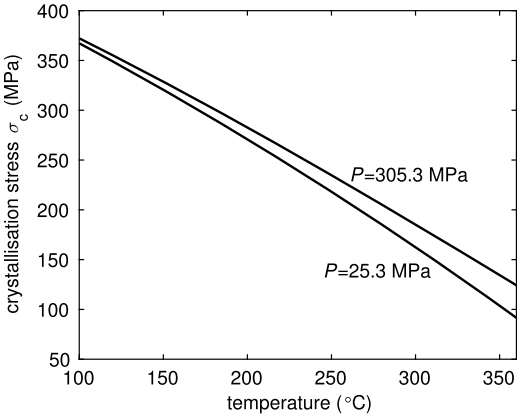

Fig. 4. Estimate of the crystallisation stress σ_c as a function of temperature and for fluid pressures of 25.3 and 305.3 MPa, computed from Eq. (2). The supersaturation Ω was approximated by the equilibrium reaction constant for the serpentinisation reaction.

Depending on the preexisting crack geometry (i.e., etch pit and serpentine wedge dimensions), the crystallisation stress might be sufficient to initiate crack propagation. An estimate of the minimum pit size c_{min} required to initiate crack growth is given by

$$c_{min} = \frac{\pi E' G_c}{4\left(\gamma(1)\sigma_c - \mu\sigma'_\infty\right)^2}, \tag{15}$$

and is plotted in Fig. 5 as a function of temperature and for far-field compressive effective stresses ranging from 0 to 200 MPa. At 300 °C and zero effective stress, the critical crack size is around 3.6 µm, and increases to around 21 µm at $\sigma'_\infty = 100$ MPa. Far from equilibrium, at temperatures less than 250 °C, and for effective stresses less than 100 MPa, the minimum crack size is of the order of a few micrometres. Such dimensions are consistent with the observed dimensions of etch pits in partially serpentinised olivine. We also note that for any stress $\sigma'_\infty \gtrsim \sigma_c$, crack propagation is impossible: the compressive stress is "clamping" the crack so that the energy release rate remains negative independently from the crack length (this is an expected result for crack growth under compressive stresses). Therefore, reaction-induced cracking appears to be

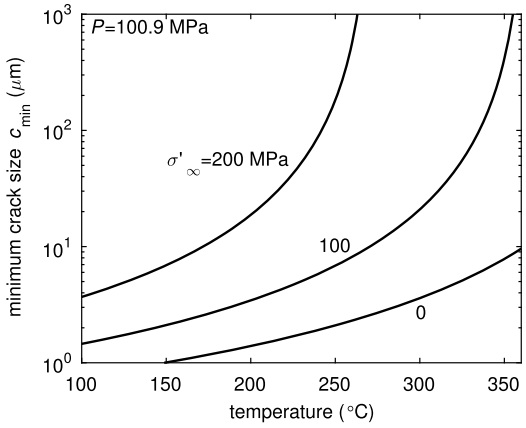

Fig. 5. Minimum crack size c_{min} beyond which spontaneous fracture propagation is possible due to crystallisation forces (Eq. (15)). All computations were performed at a constant fluid pressure of 100.9 MPa.

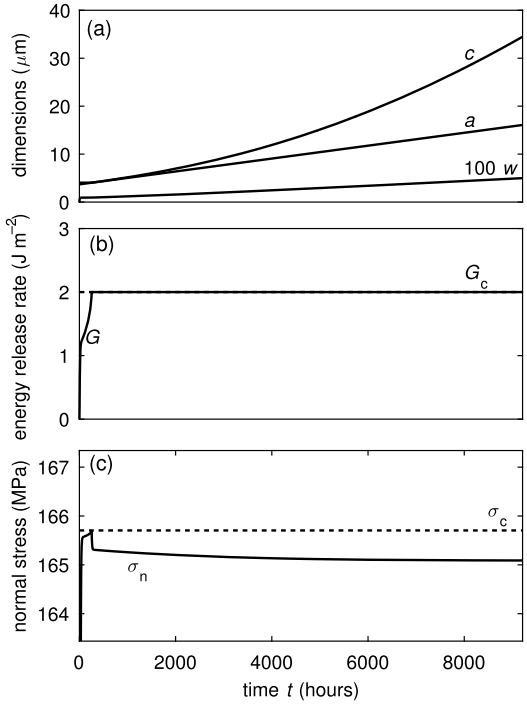

Fig. 6. Crack geometry (a), energy release rate (b) and stress (c) evolution as a function of time. In panel (a) a is the length of the serpentine mineral, c is the crack length and the serpentine wedge width w is magnified by a factor 100.

only possible at moderate effective stresses, typically at a few kilometres depth in the crust.

A representative example of the evolution of crack size and serpentine wedge dimensions is shown in Fig. 6. We use kinetic parameters from Malvoisin et al. (2012), an ambient temperature of 300 °C, fluid pressure of 50 MPa and zero effective stress. The initial conditions are set at $c(0) = 1.05 \times c_{min}$, $a(0)/c(0) = 0.8$ and $w(0) = 0$. Crack propagation starts at around 255 h, at which point the crack size c grows nonlinearly with increasing time, while the wedge dimensions (a, w) keep growing linearly. The normal stress σ_n generated by the serpentine wedge growth remains very close to, but slightly below, the crystallisation stress σ_c as the crack grows. The wedge width w is much smaller than the other dimensions of the crack, and is of the order of several 10s of nm.

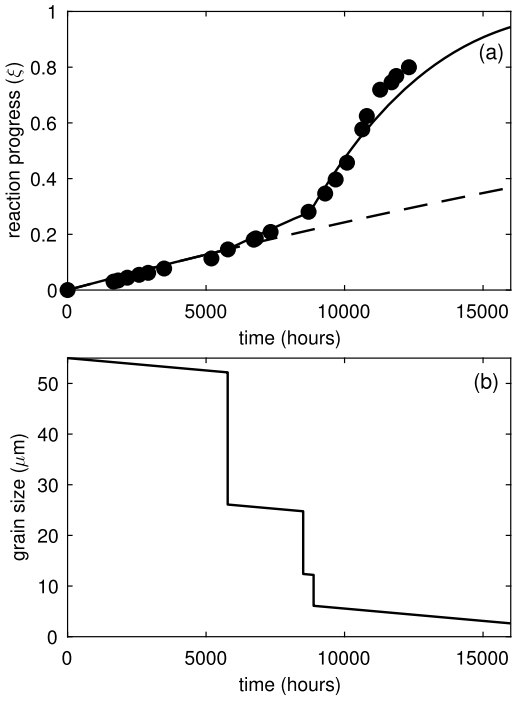

Fig. 7. Bulk reaction progress (a) and grain size (b) as a function of time, for serpentinisation of olivine at 300 °C, 50 MPa fluid pressure and zero effective stress. Black dots correspond to experimental data from Malvoisin et al. (2012). The dashed line is the reaction progress predicted when fracturing is not considered.

4. Bulk reaction rate

In the previous Section we established a model to simulate serpentinisation-induced microfracturing in a single grain. Based on this grain-scale model, we now develop a model for bulk serpentinisation with hierarchical grain fracturing. Starting from uniform cubic olivine grains of size Δ_i, the extent of the serpentinisation reaction is

$$\xi(t) = N(t)(\Delta(t)/\Delta_i)^3, \tag{16}$$

where N is the number of grains and Δ is the current grain size. This grain size evolves linearly with time due to serpentinisation at the surface of the grain,

$$\frac{d\Delta}{dt} = -2kv, \tag{17}$$

where k is the kinetic constant of the reaction, and v is the ratio of the volume of reactants (olivine) over the volume of products (serpentine), per unit mole of product. In parallel with this grain size evolution, we let surface cracks grow according to the grain-scale model, assuming that etch pits of dimensions equal to c_{min} form rapidly compared to the overall reaction progress. When the crack size reaches a given proportion of the grain size (we assume here 35%), we consider that the grain is fractured, and split it into 8 new cubes of size $\Delta/2$, and repeat the process until the grain size reaches a cutoff value below which fracturing does not occur anymore (typically 5 to 10 μm based on observations in natural samples).

Fig. 7 shows the resulting reaction progress and grain size evolution as a function of time, at a temperature of 300 °C, fluid pressure of 50 MPa and zero effective stress. The initial grain size is set to 55 μm. For comparison, experimental results at the same conditions and same initial grain size (Malvoisin et al., 2012) are also shown.

Our simple model produces remarkably accurate predictions for the serpentinisation rate. The model predicts three distinct fractur-

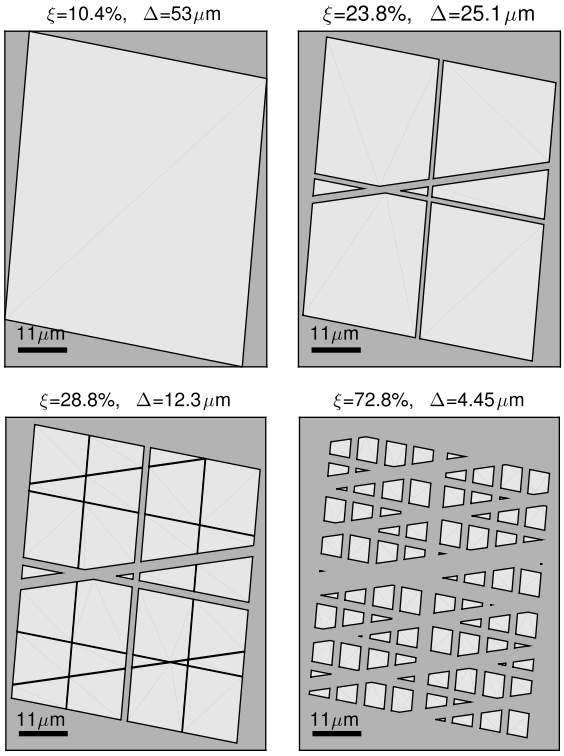

Fig. 8. Simulated texture at four different stages of the serpentinisation reaction of olivine. The model is based on cubic grains, and we show a simulated cross section across the diagonal of the initial olivine grain. Dark grey areas correspond to serpentine, light grey areas correspond to olivine. We did not account for the net volume change of the serpentinisation reaction. The olivine grain is progressively split in smaller grains during three fracturing events occurring in-between the displayed textures.

ing events (Fig. 7 b), reducing the grain size down to around 5 µm. After each event, the number of grain increases 8-fold and so does the reaction rate.

In addition to reproducing quantitatively the reaction progress, our model also predicts the texture evolution during serpentinisation. Fig. 8 shows simulated cross sections of a single olivine grain undergoing serpentinisation and being progressively fractured, according to the model predictions. The grain is initially cubic, and the simulated cross section cuts it through is long diagonal. With increasing reaction progress, we observe how the mesh texture develops, isolating olivine grains and leaving serpentine domains of variable width between them.

Our model is also run to simulate the serpentinisation of an olivine aggregate containing a realistic, nonuniform initial grain size distribution. We use the same grain size distribution as that measured in sample K3a (see Table S1), in which the degree of serpentinisation is only 5%. Every grain size fraction is run independently in the model and subsequently combined to determine the evolution of the aggregate. When computing the number of grains, we ignore grains of size less than 5 µm in order to mimic the detection level of our observations on the natural samples. The resulting bulk average reaction progress, mean grain size and total number of grains are shown in Fig. 9 a, b and c, respectively. The mean grain size tends to decrease as the reaction progresses, with an initial sharp drop at $\xi \approx 20\%$. At ξ larger than 20%, the mean grain size decreases gradually to reach around 7 µm at $\xi = 90\%$. Small variations of the grain size are superimposed to this overall trend, notably due to the rapid serpentinisation of the small grain size fractions. The evolution of the number of grains is non-monotonic, and the general trend consists in an initial increase for reaction extent up to around 40%, followed by a sharp peak and a subsequent decrease with very strong variations for reaction extent up to 90%. The evolution of the total number of grains is marked by sharp changes, which coincide with major fracturing events in the grain population. When the reaction approaches completion ($\xi > 85\%$), the number of grains becomes extremely large, since only small grains are left after episodes of reaction and fracturing.

The modelled trends of mean grain size and number of grains are similar to those observed in the natural samples (Fig. 2 a). The main difference is the sharp increase in the number of grains observed at large reaction progress, which is not observed in the natural samples (Fig. 2 c). This discrepancy is likely due to the fact that thin sections do not expose full grains but cut through them at an angle, leaving visible only a fraction of their full size. In addition, other processes not modelled here might contribute to reducing the number of grains when the grain size is very small (around 10 µm): for instance, surface energy contributions to the free energy of olivine are expected to become larger and accelerate the reaction.

5. Discussion and conclusion

Our micromechanical model is linked to a geometrical model for predicting the increase in reactive surface area due to microcracking and, thus, for estimating the evolution of bulk reaction rates. Our model has a strong predictive power, as demonstrated by the very good match between the model results and the experimental data on olivine powders (Malvoisin et al., 2012) (Fig. 7), and the formation of mesh textures as observed in natural peridotites undergoing serpentinisation. The evolution of residual olivine morphological parameters is also similar in the model and in the samples from the Marum ophiolite and the PUB, providing further evidence for a control of serpentinisation rate by reaction-induced fracturing. In the model and in the natural samples, the number of grains increases by several orders of magnitude and the grain size decreases by one order of magnitude at reaction extents below 30%, which highlights the key importance of reaction-induced fracturing in the early stages of serpentinisation. These early stages are generally not visible or quantifiable in rocks obtained from mid-ocean ridges, which are typically serpentinised to at least 20% (Rouméjon and Cannat, 2014). Here, our model results and observations on exhumed ophiolite samples confirm that reaction-induced fracturing is a key mechanism of fluid pathways generation at mid-ocean ridges. This is in part due to the low effective pressure operating in the subsurface of the oceanic crust, which allow fractures to propagate. Another evidence for the control of fracturing by reaction is the preservation of a shape preferred fracture orientation up to 70% of reaction progress. Two main orientations at 90° to each other are recorded, indicating hierarchical fracturing (Bohn et al., 2005), a typical feature of reaction-induced cracking (Iyer et al., 2008). The fracture preferred orientation is progressively lost at reaction progresses above 40% due to grain rounding by dissolution when cracking does not occur anymore (Fig. 2). These observations are in agreement with both the observations of hierarchical fracturing at low reaction progress in peridotites (Iyer et al., 2008; Kelemen et al., 2011), and the scarcity of three orthogonal veins at higher reaction progresses (Rouméjon and Cannat, 2014).

The model predictions are also strengthened by the use of well-constrained geometry and parameters. Following Plümper et al. (2012), cracks are assumed to initiate from etch pits which are dissolution features commonly formed during olivine weathering (e.g. Velbel, 2009) or serpentinisation (Malvoisin et al., 2012; Plümper et al., 2012; Rouméjon and Cannat, 2014; Klein et al., 2015; Lisabeth et al., 2017). Etch pits are also observed in the samples from the Marum ophiolite and the PUB studied here (Fig. 1 a, b, c and d), and found to serve for reaction-induced cracking initiation.

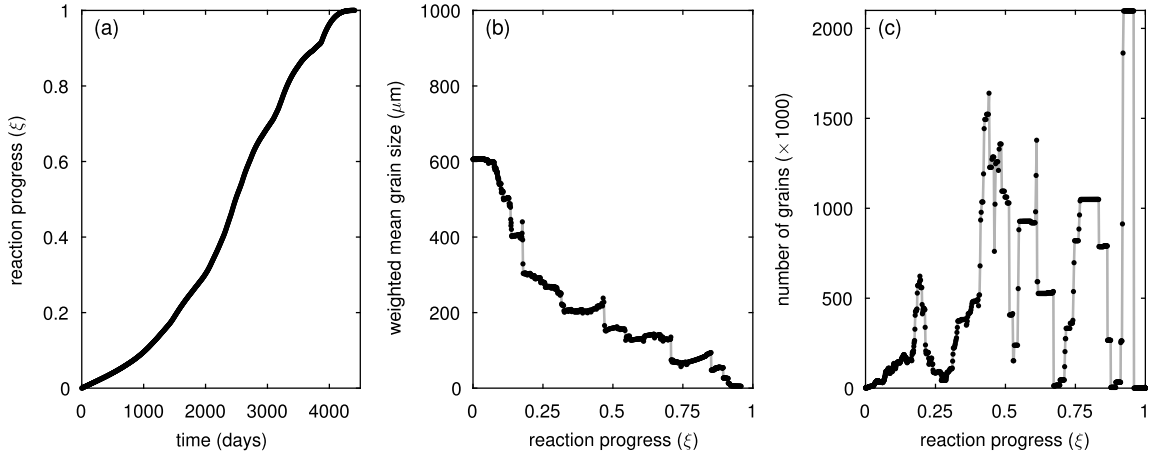

Fig. 9. Simulated evolution of reaction progress (a) as a function of time and weighted mean grain size (b) and number of grains (c) as a function of reaction progress predicted with the model for bulk reaction rate. The initial grain size distribution is taken from image analysis on sample K03a. As for the study of natural samples, grains smaller than 5 μm are not considered for statistical analysis.

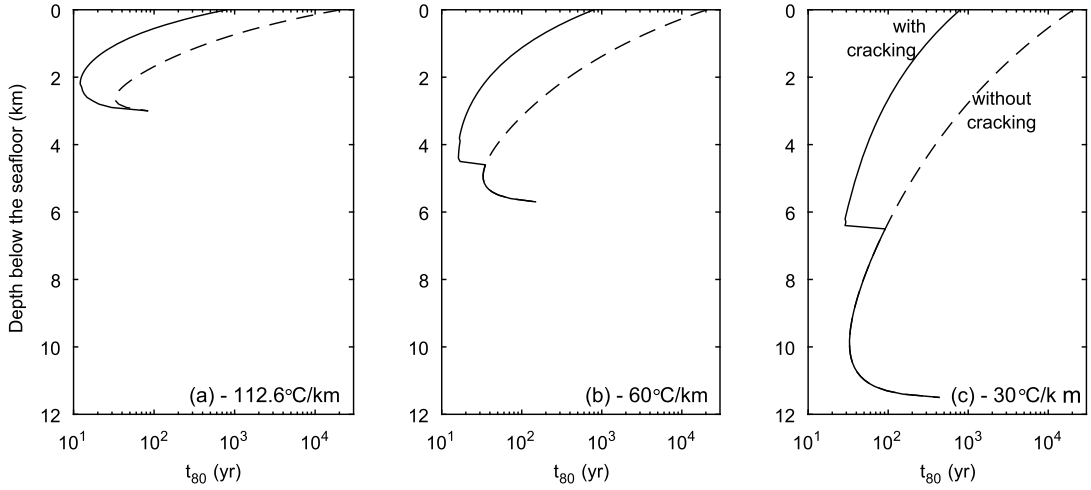

Fig. 10. Model predictions for the time needed to reach 80% of reaction progress (t_{80}) as a function of the depth below the seafloor for geothermal gradients of 112.6 (a), 60 (b) and 30 °C/km (c). Predictions with (plain lines) and without (dashed lines) reaction-induced cracking are both shown.

In samples with the lowest reaction extent, etch pits preferentially developed at the contact between olivine and spinel probably due to higher serpentinisation rate in the presence of aluminum-bearing minerals Andreani et al. (2013). Numerous radial micro-cracks were also observed around spinels (Fig. 1 e and f) providing more evidence for the genetic link between etch pits formation and reaction-induced fracturing.

The model uses only six parameters: three related to well-constrained olivine properties (dissolution rate, elastic parameters, and critical energy release rate), the crystallisation pressure, and two geometrical parameters. The crystallisation pressure is calculated for the maximum possible supersaturation. Thermodynamic calculations indicates crystallisation pressure of the order of several hundreds of MPa (Fig. 4). Even if such stresses are higher than the fracture strength of crustal rocks (Kelemen and Hirth, 2012), they are not necessary sufficient to reach the critical energy release rate due to small initial crack length and/or high compressive effective stresses (Fig. 5). For the etch pits size measured in the samples from the Marum ophiolite and the PUB, micro-cracks are not expected to propagate for compressive effective stresses above approximately 100 MPa (Fig. 5). Amid the geometrical parameters, the number of grains formed at each subdivision step is chosen as the simplest one (8 grains per step) whereas the proportion of crack length to grain size necessary for subdivision to occur is the only free parameter of the model.

The good match between the model results and the observations, as well as the use of a limited number of well-constrained parameters, allow us to use our model with reasonable confidence to predict serpentinisation rates nature. Our model is thus used to predict a characteristic serpentinisation time (t_{80}, defined as the time required to serpentinise olivine to 80%) in oceanic peridotites. We use an initial grain size of 500 μm and consider a hydrostatic fluid pressure gradient (Fig. 10). Three different geothermal gradients of 30, 60 and 112.6 °C/km are used to represent different lithospheric age. The maximum value of 112.6 °C/km corresponds to a measurement in an active oceanic core complex at the Atlantis massif (Blackman et al., 2014). When reaction-induced fracturing does not occur, t_{80} decreases with depth from 10,000 yr on the seafloor to reach a minimum of 30 yr at approximately 2.2, 5.1 and 10 km depth for geothermal gradients of 112.6, 60 and 30 °C/km, respectively. When reaction-induced fracturing is allowed, t_{80} is reduced by one order of magnitude. For instance, in the case of a geothermal gradient of 112.6 °C/km, we obtain a maximum in t_{80} of only 1000 yr at the surface and a minimum of 12 yr at 2.2 km depth. At a fixed temperature, the effective pressure is higher for cool than for hot geothermal gradients, restricting the domain where reaction-induced fracturing can occur (Eq. (15)). As a result, reaction-induced fracturing occurs at all depths with a geothermal gradient of 112.6 °C/km whereas it is restricted to the first 6 kilometres of the crust with a geothermal gradient of

30 °C/km. This is also responsible for a shift of the maximum serpentinisation rate towards shallower depths of 4.5 and 6.4 km for geothermal gradients of 60 and 30 °C/km, respectively. A shift in the depth of the minimum t_{80} by 0.4 km is also observed for the maximum geothermal gradient but it related to the increase of crystallisation pressure at low temperature far from the equilibrium.

The predictions provided by the model have strong implications regarding serpentinisation on the seafloor. First, they indicate that the time required for serpentinisation is one to three orders of magnitude smaller than the estimated duration of hydrothermal activity in ultramafic-hosted hydrothermal systems (Früh-Green et al., 2003). These results are in good agreement with the overall high reaction progress measured in serpentinised peridotites recovered at mid-ocean ridges (Oufi et al., 2002; Rouméjon and Cannat, 2014). The sporadic occurrence of samples less extensively serpentinised may indicate a limited or transient availability of water at mid-ocean ridges due to processes such as porosity clogging as a result of volume increase during reaction (Farough et al., 2016). For hot geothermal gradients near the ridge axis (at least 60 °C/km), serpentinisation is expected to occur at depth below 6 km, in agreement with the depth at which low P-waves velocities are measured on the Mid-Atlantic ridge (Canales et al., 2000; Cannat et al., 2010). Our model also indicates that serpentinisation can occur down to depths of 12 km for a cold geothermal gradient far from the ridge axis or in magma-poor environments. Interestingly, the lithosphere was recently found to be aseismic at ultraslow-spreading ridges up to depths of 15 km suggesting significant serpentinisation up to these depths (Schlindwein and Schmid, 2016).

Although our model provides the best up-to-date quantitative estimate of serpentinisation rate on the seafloor and in ophiolites, its use at high pressure, for example for mantle wedge hydration in subduction zones, is fraught with uncertainty. First, the serpentine mineral formed during serpentinisation at high pressure is antigorite, which might imply different mineralogical processes and reaction kinetics compared to lizardite (used in our model). Secondly, the effective pressure remains mostly unconstrained in subduction zones and in the overlying mantle wedge; as shown here, the effective pressure has a key role in preventing or allowing micro-cracking, so that uncertainties in this parameter have a strong impact on the modelled serpentinisation rate. Finally, the initial grain size used in our model (approximately 500 µm) is smaller than the size of the domains with the same crystallographic orientation thought to represent the initial olivine crystals (up to several centimetres, Kaczmarek et al., 2015). Thermal cracking has been shown to generate the first fluid pathways in these crystals at mid-ocean ridges and in ophiolites (Rouméjon and Cannat, 2014). For the largest crystals observed in the samples from the Marum ophiolite and the PUB (1 cm), the reactive surface area is multiplied by 20 during thermal cracking down to 500 µm. Pronounced thermal cracking is not expected to occur in subduction zones where mantle rocks are neither exhumed nor cooled rapidly by hydrothermal circulation. In this context, the serpentinisation rate might thus be overestimated by several orders of magnitude.

Acknowledgements

The authors thank P. Vonlanthen for technical assistance with Scanning Electron Microscopy, and G. Hetényi and B. Putlitz for discussions. The careful reviews and comments by O. Plümper and P.B. Kelemen were also much appreciated for helping to improve the manuscript. BM acknowledges support from the Swiss National Science Foundation (Ambizione grant No. PZ00P2_168083). NB acknowledges support from the Natural Environment Research Council (grants NE/K009656/1 and NE/M016471/1). The

Matlab codes used in our numerical simulations can be found at www.github.com/nbrantut/Serpentinisation.git.

Appendix A. Supplementary material

Supplementary material related to this article can be found online at http://dx.doi.org/10.1016/j.epsl.2017.07.042.

References

Abramson, E.H., Brown, M., Slutsky, L.J., Zaug, J., 1997. The elastic constants of San Carlos olivine up to 17 GPa. J. Geophys. Res. 102 (B6). 12523–12263.
Allen, D.E., Seyfried, W.E., 2004. Serpentinization and heat generation: constraints from Lost City and Rainbow hydrothermal systems. Geochim. Cosmochim. Acta 68 (6), 1347–1354.
Andreani, M., Daniel, I., Pollet-Villard, M., 2013. Aluminum speeds up the hydrothermal alteration of olivine. Am. Mineral. 98 (10), 1738–1744.
Atkinson, B.K., 1984. Subcritical crack growth in geological materials. J. Geophys. Res. 89 (B6), 4077–4114.
Auzende, A.L., Daniel, I., Reynard, B., Lemaire, C., Guyot, F., 2004. High-pressure behaviour of serpentine minerals: a Raman spectroscopic study. Phys. Chem. Miner. 31 (5), 269–277.
Blackman, D.K., Slagle, A., Guerin, G., Harding, A., 2014. Geophysical signatures of past and present hydration within a young oceanic core complex. Geophys. Res. Lett. 41 (4), 1179–1186.
Bohn, S., Douady, S., Couder, Y., 2005. Four sided domains in hierarchical space dividing patterns. Phys. Rev. Lett. 94 (5), 054503.
Boudier, F., Baronnet, A., Mainprice, D., 2010. Serpentine mineral replacements of natural olivine and their seismic implications: oceanic lizardite versus subduction-related antigorite. J. Petrol. 51 (1–2), 495–512.
Canales, J.P., Collins, J.A., Escartín, J., Detrick, R.S., 2000. Seismic structure across the rift valley of the Mid-Atlantic Ridge at 23°20′ (MARK area): implications for crustal accretion processes at slow spreading ridges. J. Geophys. Res. 105 (B12), 28411–28425.
Cannat, M., Fontaine, F., Escartín, J., 2010. Serpentinization and associated hydrogen and methane fluxes at slow spreading ridges. In: Rona, P.A., Devey, C.W., Dyment, J., Murton, B.J. (Eds.), Diversity of Hydrothermal Systems on Slow Spreading Ocean Ridges. In: Geophys. Monogr. Ser., vol. 188. American Geophysical Union, Washington, DC, pp. 241–264.
Correns, C.W., 1949. Growth and dissolution of crystals under linear pressure. Discuss. Faraday Soc. 5, 267–271.
Demartin, B., Hirth, G., Evans, B., 2004. Experimental constraints on thermal cracking of peridotite at oceanic spreading centers. In: German, C., Lin, J., Parson, L. (Eds.), Mid-Ocean Ridges. In: Geophys. Monogr. Ser., vol. 148. American Geophysical Union, Washington, DC, pp. 167–185.
Escartín, J., Hirth, G., Evans, B., 2001. Strength of slightly serpentinized peridotites: implications for the tectonics of oceanic lithosphere. Geology 29, 1023–1026.
Farough, A., Moore, D.E., Lockner, D.A., Lowell, R.P., 2016. Evolution of fracture permeability of ultramafic rocks undergoing serpentinization at hydrothermal conditions: an experimental study. Geochem. Geophys. Geosyst. 17, 44–55.
Fisher, N.I., 1993. Statistical Analysis of Circular Data. Cambridge University Press, Cambridge, UK.
Fletcher, R.C., Merino, E., 2001. Mineral growth in rocks: kinetic-rheological models of replacement, vein formation, and syntectonic crystallization. Geochim. Cosmochim. Acta 65 (21), 3733–3748.
Frost, B.R., 1985. On the stability of sulfides, oxides and native metals in serpentinite. J. Petrol. 26 (1), 31–63.
Früh-Green, G.L., Kelley, D.S., Bernasconi, S.M., Jeffrey, A., Ludwig, K.A., Butterfield, D.A., Boschi, C., Proskurowski, G., 2003. 30,000 years of hydrothermal activity at the Lost City vent field. Science 301 (5632), 495–498.
Godard, M., Luquot, L., Andreani, M., Gouze, P., 2013. Incipient hydration of mantle lithosphere at ridges: a reactive-percolation experiment. Earth Planet. Sci. Lett. 371, 92–102.
Hövelmann, J., Austrheim, H., Jamtveit, B., 2012. Microstructure and porosity evolution during experimental carbonation of a natural peridotite. Chem. Geol. 334, 254–265.
Iyer, K., Jamtveit, B., Mathiesen, J., Malthe-Sørensen, A., Feder, J., 2008. Reaction-assisted hierarchical fracturing during serpentinization. Earth Planet. Sci. Lett. 267 (3–4), 503–516.
Jamtveit, B., Putnis, C., Malthe-Sørensen, A., 2009. Reaction induced fracturing during replacement processes. Contrib. Mineral. Petrol. 157 (1), 127–133.
Johnson, J.W., Oelkers, E.H., Helgeson, H.C., 1992. SUPCRT92: a software package for calculating the standard molal thermodynamic properties of minerals, gases and aqueous species, and reactions for 1 to 5000 bar and 0 to 1000 °C. Comput. Geosci. 18 (7), 899–947.
Kaczmarek, M.-A., Jonda, L., Davies, H.L., 2015. Evidence of melting, melt percolation and deformation in a supra-subduction zone (Marum ophiolite complex, Papua New Guinea). Contrib. Mineral. Petrol. 170 (2), 19.

Kelemen, P.B., Hirth, G., 2012. Reaction-driven cracking during retrograde metamorphism: olivine hydration and carbonation. Earth Planet. Sci. Lett. 345–348, 81–89.

Kelemen, P.B., Matter, J., 2008. In situ carbonation of peridotite for CO_2 storage. Proc. Natl. Acad. Sci. 105 (45), 17295–17300.

Kelemen, P.B., Matter, J., Streit, E.E., Rudge, J.F., Curry, W.B., Blusztajn, J., 2011. Rates and mechanisms of mineral carbonation in peridotite: natural processes and recipes for enhanced, in situ CO_2 capture and storage. Annu. Rev. Earth Planet. Sci. 39, 545–576.

Klein, F., Bach, W., Humphris, S.E., Kahl, W.-A., Jöns, N., Moskowitz, B., Berquó, T.S., 2014. Magnetite in seafloor serpentinite – some like it hot. Geology 42 (2), 135–138.

Klein, F., Grozeva, N.G., Seewald, J.S., McCollom, T.M., Humphris, S.E., Moskowitz, B., Berquó, T.S., Kahl, W.-A., 2015. Fluids in the Crust. Experimental constraints on fluid-rock reactions during incipient serpentinization of harzburgite. Am. Mineral. 100 (4), 991–1002.

Lasaga, A.C., 1981. Transition state theory. In: Lasaga, A.C., Kirkpatrick, R.J. (Eds.), Kinetics of Geochemical Processes. Min. Soc. Am., Washington, DC, pp. 135–169.

Lisabeth, H.P., Zhu, W., Kelemen, P.B., Ilgen, A., 2017. Experimental evidence for chemo-mechanical coupling during carbon mineralization in ultramafic rocks. Earth Planet. Sci. Lett. 474, 355–367.

Lus, W.Y., McDougall, I., Davies, H.L., 2004. Age of the metamorphic sole of the Papuan Ultramafic Belt ophiolite, Papua New Guinea. Tectonophysics 392 (1), 85–101.

Macdonald, A.H., Fyfe, W.S., 1985. Rate of serpentinization in seafloor environments. Tectonophysics 116 (1), 123–135.

Malvoisin, B., 2015. Mass transfer in the oceanic lithosphere: serpentinization is not isochemical. Earth Planet. Sci. Lett. 430, 75–85.

Malvoisin, B., Brunet, F., 2014. Water diffusion-transport in a synthetic dunite: consequences for oceanic peridotite serpentinization. Earth Planet. Sci. Lett. 403, 263–272.

Malvoisin, B., Brunet, F., Carlut, J., Rouméjon, S., Cannat, M., 2012. Serpentinization of oceanic peridotites: 2. Kinetics and processes of San Carlos olivine hydrothermal alteration. J. Geophys. Res. 117.

Martin, B., Fyfe, W.S., 1970. Some experimental and theoretical observations on the kinetics of hydration reactions with particular reference to serpentinization. Chem. Geol. 6, 185–202.

Moody, J.B., 1976. Serpentinization: a review. Lithos 9 (2), 125–138.

Oufi, O., Cannat, M., Horen, H., 2002. Magnetic properties of variably serpentinized abyssal peridotites. J. Geophys. Res. 107 (B5).

Paterson, M.S., 1973. Nonhydrostatic thermodynamics and its geologic applications. Rev. Geophys. Space Phys. 11 (2), 355–389.

Plümper, O., Røyne, A., Magrasò, A., Jamtveit, B., 2012. The interface-scale mechanism of reaction-induced fracturing during serpentinization. Geology 40 (12), 1103–1106.

Rouméjon, S., Cannat, M., 2014. Serpentinization of mantle-derived peridotites at mid-ocean ridges: mesh texture development in the context of tectonic exhumation. Geochem. Geophys. Geosyst. 15 (6), 2354–2379.

Røyne, A., Meakin, P., Malthe-Sørenssen, A., Jamtveit, B., Dysthe, D.K., 2011. Crack propagation driven by crystal growth. Europhys. Lett. 96 (2), 24003. 1–6.

Rudge, J.F., Kelemen, P.B., Spiegelman, M., 2010. A simple model of reaction-induced cracking applied to serpentinization and carbonation of peridotite. Earth Planet. Sci. Lett. 291 (1–4), 215–227.

Rüpke, L.H., Morgan, J.P., Hort, M., Connolly, J.A.D., 2004. Serpentine and subduction zone water cycle. Earth Planet. Sci. Lett. 223 (1–2), 17–34.

Schlindwein, V., Schmid, F., 2016. Mid-ocean-ridge seismicity reveals extreme types of ocean lithosphere. Nature 535 (7611), 276–279.

Seyfried, W.E., Foustoukos, D.I., Fu, Q., 2007. Redox evolution and mass transfer during serpentinization: an experimental and theoretical study at 200 °C, 500 bar with implications for ultramafic-hosted hydrothermal systems at mid-ocean ridges. Geochim. Cosmochim. Acta 71 (15), 3872–3886.

Sleep, N.M., Meibom, A., Fridriksson, T., Coleman, R.G., Bird, D.K., 2004. H_2-rich fluids from serpentinization: geochemical and biotic implications. Proc. Natl. Acad. Sci. USA 101 (35), 12818–12823.

Steiger, M., 2005. Crystal growth in porous materials – I: The crystallization pressure of large crystals. J. Cryst. Growth 282 (3–4), 455–469.

Tada, H., Paris, P.C., Irwin, G.R., 2000. The Stress Analysis of Cracks Handbook, 3rd edition. ASME Press, New York.

Tauzin, B., Reynard, B., Perrillat, J.-P., Debayle, E., Bodin, T., 2017. Deep crustal fracture zones control fluid escape and the seismic cycle in the Cascadia subduction zone. Earth Planet. Sci. Lett. 460, 1–11.

Toft, P.B., Arkani-Hamed, J., Haggerty, S.E., 1990. The effects of serpentinization on density and magnetic susceptibility: a petrophysical model. Phys. Earth Planet. Inter. 65 (1–2), 137–157.

Tucholke, B.E., Lin, J., 1994. A geological model for the structure of ridge segments in slow spreading ocean crust. J. Geophys. Res. 99 (B6), 11937–11958.

Tutolo, B.M., Mildner, D.F.R., Gagnon, C.V.L., Martin, O., Seyfried, W.E., 2016. Nanoscale constraints on porosity generation and fluid flow during serpentinization. Geology 44 (2), 103–166.

Velbel, M.A., 2009. Dissolution of olivine during natural weathering. Geochim. Cosmochim. Acta 73 (20), 6098–6113.

Wegner, W.W., Ernst, W.G., 1983. Experimentally determined hydration and dehydration reaction rate in the system $MgO–SiO_2–H_2O$. Am. J. Sci. 283-A, 151–180.

Wicks, F.J., Whittaker, E.J.W., 1977. Serpentine texture and serpentinization. Can. Mineral. 15, 459–488.